Fountain Flow Revisited: The Effect of Various Fluid Mechanics Parameters

Evan Mitsoulis
School of Mining Engineering and Metallurgy, National Technical University of Athens, Zografou, 157 80, Athens, Greece

DOI 10.1002/aic.12038
Published online November 17, 2009 in Wiley InterScience (www.interscience.wiley.com).

Numerical simulations have been undertaken for the benchmark problem of fountain flow present in injection-mold filling. The finite element method (FEM) is used to provide numerical results for both cases of planar and axisymmetric domains under laminar, isothermal, steady-state conditions for Newtonian fluids. The effects of inertia, gravity, surface tension, compressibility, slip at the wall, and pressure dependence of the viscosity are all considered individually in parametric studies covering a wide range of the relevant parameters. These results extend previous ones regarding the shape of the front, and in particular the centerline front position, as a function of the dimensionless parameters. The pressures from the simulations have been used to compute the excess pressure losses in the system (front pressure correction or exit correction). Inertia leads to highly extended front positions relative to the inertialess Newtonian values, which are 0.895 for the planar case and 0.835 for the axisymmetric one. Gravity acting in the direction of flow shows the same effect, while gravity opposing the flow gives a reduced bulge of the fountain. Surface tension, slip at the wall, and compressibility, all decrease the shape of the front. Pressure-dependence of the viscosity leads to increased front position as a corresponding dimensionless parameter goes from zero (no effect) to higher values of the pressure-shift factor. The exit correction increases monotonically with inertia, compressibility, and gravity, while it decreases monotonically with slip and pressure-dependence of the viscosity. Contour plots of the primary variables (velocity-pressure) show interesting trends compared with the base case (zero values of the dimensionless parameters and of surface tension). © 2009 American Institute of Chemical Engineers *AIChE J,* 56: 1147–1162, 2010
Keywords: fountain flow, exit correction, injection molding, inertia, gravity, surface tension, compressibility, wall slip, pressure-dependence of viscosity, Newtonian fluid

Introduction

Fountain flow is a well-known fluid-mechanics phenomenon present in all cases where a moving fluid displaces another immiscible fluid.[1] Within the context of non-Newtonian fluid mechanics, this type of flow is of interest in polymer processing, and in particular in the flow of polymer melts in injection-mold filling.[2] The theoretical problem has been adequately addressed in the mid-80's by a number of researchers,[3–5] starting with the pioneering work of Mavridis et al.[3] who for the first time calculated correctly the front position. These works dealt primarily with Newtonian fluids and showed intricate patterns developing when tracing particles, in agreement with experiments.[3–6] Mavridis et al.[3] showed in a sample run (for a power-law index of $n = 0.5$) that power-law fluids only slightly affect the position of the flow front. Beris[7] argued that fountain flow patterns (especially the observed V-shapes[8]) are independent of the model

Correspondence concerning this article should be addressed to E. Mitsoulis at mitsouli@metal.ntua.gr

and form as a consequence of fluid-mechanics principles that the fluid obeys at the front. More recently, Bogaerds et al.[9] performed calculations with a viscoelastic model (the extended pom-pom[10]), and showed that the flow front is not affected appreciably by the elasticity of the polymer melt, and it does not deviate much from a semicircle for a wide range of flow rates in a planar domain. All these works have shown that the results range from 0.8 to 1.05 of the radius of the semicircle, with the lower values corresponding to the axisymmetric case of a Newtonian fluid, while shear-thinning of power-law fluids brings the results closer to a semicircle front.

Although the problem is well understood from the physics and fluid mechanics points of view, it has become evident that numerically subtle differences exist for different fluid models and types of domain geometry (planar vs. axisymmetric). The problem of finding the free surface in fountain flow is not as easy as in the extrudate swell case,[11] and special care must be taken when constructing the domain discretization with finite elements, the method of choice for this problem. Powerful methods for tackling free-surface problems have been developed, such as the spine method,[12] the arbitrary Lagrangian-Eulerian (ALE) method[13] and its variants,[14] the volume-of-fluid (VOF) method,[15] the level-set method,[16] to name just a few. The rheology of the fluids, especially with highly nonlinear models, may also interact in unpredictable ways. The same is true for other parameters influencing the fluid mechanics of fountain flow, ranging from inertia, to gravity, to surface tension, etc.

The key work of Coyle et al.[4] showed both experimentally and computationally that the influence of gravity and surface tension has a pronounced effect on the flow front, reducing it appreciably when gravity opposes the flow. Since then, no other work has addressed the influence of some standard fluid mechanics parameters in fountain flow in a parameter range. It, is, therefore, the purpose of this article to revisit the problem of fountain flow for a full parametric study of Newtonian fluids in both planar and axisymmetric geometries, and study the effects of inertia, gravity (both opposing and aiding the flow), compressibility, a pressure-dependent viscosity, slip at the wall, and surface tension on the free surface. The emphasis will be on providing detailed results both for the free surface location and the excess pressure in the system as a function of the relevant fluid mechanics dimensionless parameters.

Mathematical Modeling

Governing equations

The problem at hand is shown schematically in Figure 1, where a fluid is considered advancing with an average velocity U, in a stationary frame of reference and thus the process is considered as steady-state.[9]

Many materials used in injection molding are non-Newtonian, exhibiting either *pseudoplastic* (shear-thinning or -thickening) or *viscoplastic* (presence of a yield stress) behavior (see, e.g., Bird et al.[17]). A recent article[18] addresses these issues of non-Newtonianness. Here we concentrate on the Newtonian fluid model and study the effect that various fluid mechanics parameters have on the fountain flow.

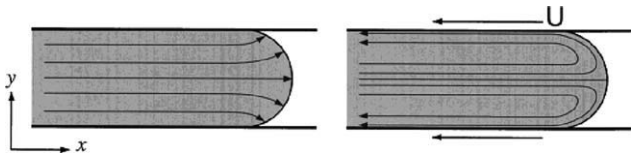

Figure 1. Schematic representation of fountain flow showing the kinematics pattern.[9]

Reference frame of mold (left), and reference frame of the moving interface (right).

For isothermal flows, the conservation of energy equation is not considered and the temperature does not enter into the system of the Navier-Stokes conservation equations. These are:

- Mass conservation (including density changes for compressible fluids)

$$\nabla \cdot (\rho \overline{u}) = 0. \tag{1}$$

- Momentum conservation (including effects of inertia, pressure, viscous and gravity forces)

$$\rho \overline{u} \cdot \nabla \overline{u} = -\nabla p + \nabla \cdot \overline{\overline{\tau}} + \rho \overline{g}. \tag{2}$$

For compressible fluids, we have

$$\overline{\overline{\tau}} = \mu\left(\nabla \overline{u} + \nabla \overline{u}^{\mathrm{T}}\right) - \frac{2\mu}{3}(\nabla \cdot \overline{u})\overline{\overline{I}}. \tag{3}$$

In the aforementioned, ρ is the density, $\overline{u}$ is the velocity vector, p is the pressure, $\overline{\overline{\tau}}$ is the extra-stress tensor, μ is the viscosity, $\overline{g}$ is the acceleration of gravity, and $\overline{I}$ the unit tensor. In the aforementioned, we have assumed that we deal with dense fluids, which have a zero dilatational (bulk) viscosity.[2]

Also for compressible fluids, density and pressure are related via a simple thermodynamic equation of state, either linear or exponential.[19] The linear form is given by

$$\rho = \rho_0[1 + \beta(p - p_0)], \tag{4}$$

where β is the isothermal compressibility coefficient at reference pressure p_0 also related to reference density ρ_0.

Similarly, the viscosity can be a function of pressure, either linear or exponential.[20] The exponential form is given by[21]

$$\mu = \mu_0 \exp[\beta_p(p - p_0)], \tag{5}$$

where β_p is the pressure-shift coefficient at reference pressure p_0 also related to reference viscosity μ_0.

The constitutive equation for Newtonian fluids (Eq. 3) is substituted into the momentum equations (Eq. 2), and the equation of state (Eq. 4) into both the continuity (Eq. 1) and momentum equations. The whole system of conservation equations must be solved along with appropriate boundary conditions. Figure 2 shows the solution domain and boundary conditions for the axisymmetric geometry. Because of symmetry, only one half of the flow domain is considered,

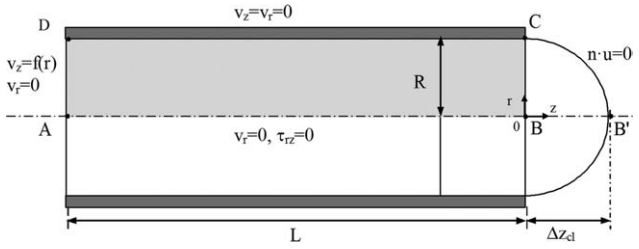

Figure 2. Schematic diagram of flow domain in a stationary frame of reference and boundary conditions.

as was done previously.[3–6] The boundary conditions are, therefore (see Figure 2):

- symmetry along AB ($v_r = 0$, $\tau_{rz} = 0$),
- no slip along the walls CD ($v_z = v_r = 0$),
- along the inflow boundary DA, a fully developed Poiseuille velocity profile corresponding to a unit average velocity U ($v_z(r) = 2(1-r^2)$, $v_r = 0$),
- along the free surface BC, vanishing tangential and normal stresses ($(\overline{\overline{\sigma}} \cdot \overline{n}) \cdot \overline{t} = 0$, $(\overline{\overline{\sigma}} \cdot \overline{n}) \cdot \overline{n} = 0$), and no flow through the surface ($\overline{n} \cdot \overline{u} = 0$), where $\overline{n}$ and $\overline{t}$ are the normal and tangential vectors to the surface, and $\overline{\overline{\sigma}} = -p\overline{\overline{I}} + \overline{\overline{\tau}}$ is the total stress.

In the case of slip at the wall, the normal velocity is set to 0, and the tangential velocity obeys a linear slip law.[22] Therefore, along the walls CD we have

$$\overline{t} \cdot \overline{u} = \beta_{sl}(\overline{t}\overline{n} : \overline{\overline{\tau}}), \qquad \overline{n} \cdot \overline{u} = 0, \tag{6}$$

where β_{sl} is a slip coefficient. Accordingly, the inlet Poiseuille velocity profile is modified to accommodate the slip law based on its analytical solution with slip.[19,22]

In the case of surface tension on the free-surface BC, there are still vanishing tangential stresses ($(\overline{\overline{\sigma}} \cdot \overline{n}) \cdot \overline{t} = 0$), and no flow through the surface ($\overline{n} \cdot \overline{u} = 0$), but the normal stresses satisfy a force equilibrium according to[23,24]

$$(\overline{\overline{\sigma}} \cdot \overline{n}) \cdot \overline{n} = -2R_c\gamma - p_0, \tag{7}$$

where γ is the surface tension, p_0 is the reference pressure (set to 0), and $2R_c$ is the mean curvature of the free surface given by[23,24]

$$-2R_c = \frac{h_{zz}}{\left[1 + h_z^2\right]^{3/2}} - \frac{1}{r\sqrt{1 + h_z^2}}. \tag{8}$$

In Eq. 8, the subscripts z and zz denote first- and second-order differentiation of the free-surface location h with respect to z, and r is the local radius. The second term is 0 in planar flows.

Previous numerical experiments[18] for setting a reference pressure as a boundary condition showed that the best solution is obtained by not specifying anywhere a reference pressure. However, in the equations the reference pressure p_0 is set to 0.

All lengths are scaled with the radius R in axisymmetric geometry, or with H in planar geometry, all velocities with the average velocity U, and all pressures and stresses with $\mu U/R$ or $\mu U/H$, respectively.

Dimensionless numbers

The relevant dimensionless numbers of the Navier-Stokes equations need a characteristic length L, and a characteristic velocity U. In this case these are the channel half gap H (or radius R for axisymmetric flows), and the average incoming velocity. The following numbers are defined, arising from *field flow*:

The Reynolds number, Re, is a measure of inertia forces over viscous forces

$$Re = \frac{\rho UR}{\mu}. \tag{9}$$

When $Re = 0$, we have inertialess flow. In the current simulations $0 \le Re \le 7$.

The Stokes number, St, is a measure of gravity forces over viscous forces

$$St = \frac{\rho g R^2}{\mu U}. \tag{10}$$

When $St = 0$, we have no gravity effects. In the current simulations, $0 \le St \le 40$.

The compressibility coefficient B, is a measure of fluid compressibility:

$$B = \frac{\beta \mu U}{R}. \tag{11}$$

When $B = 0$, we have incompressible flow. In the current simulations, $0 \le B \le 0.12$.

The pressure-shift coefficient B_p, is a measure of pressure-dependence of the fluid viscosity

$$B_p = \frac{\beta_p \mu U}{R}. \tag{12}$$

When $B_p = 0$, we have no pressure-dependence of the viscosity. In the current simulations, $0 \le B_p < 0.1$.

Also, the following dimensionless numbers arise due to *boundary flow*.

The slip coefficient B_{sl}, is a measure of fluid slip at the wall

$$B_{sl} = \frac{\beta_{sl}\mu}{R}. \tag{13}$$

When $B_{sl} = 0$, we have no-slip conditions. When $B_{sl} \approx 1$, we have macroscopically obvious slip. In the current simulations, $0 \le B_{sl} \le 100$.

The capillary number, Ca, is a measure of surface tension over viscous effects

$$Ca = \frac{\mu U}{\gamma}. \tag{14}$$

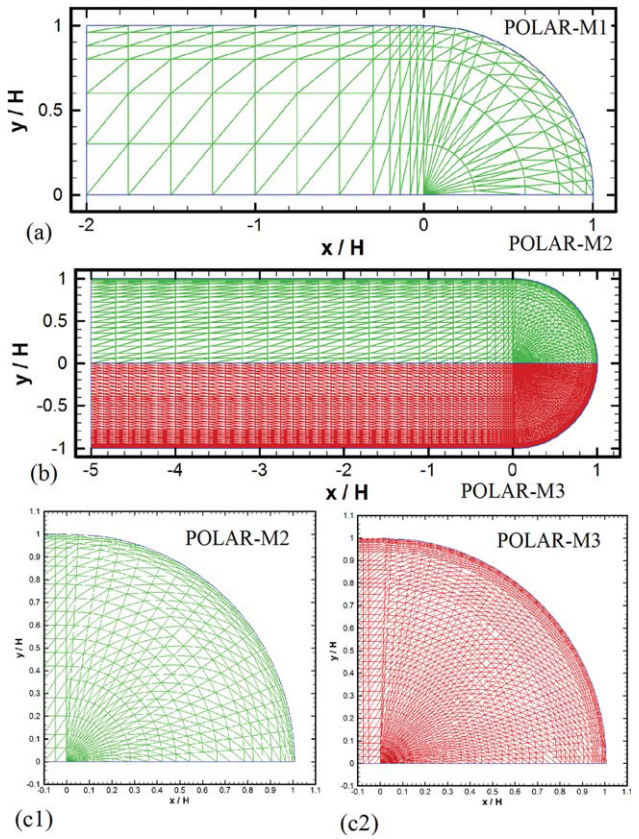

Figure 3. Polar finite element meshes used in the current computations: (a) POLAR-M1 also used by Mavridis et al.[3] (b) upper half shows POLAR-M2, while lower half shows POLAR-M3, and (c) blow-up of the flow front - (c1) of POLAR-M2, (c2) of POLAR-M3.

The meshes shown use a semicircle as an initial guess for the flow front. Table 1 gives the various mesh characteristics. [Color figure can be viewed in the online issue, which is available at www.interscience.wiley.com.]

When $Ca \to \infty$, viscous forces dominate, as is the case with very viscous fluids. When $Ca \to 0$, surface tension dominates, as is the case with very low-viscosity fluids. In the current simulations, $10{,}000 \leq Ca < 0.02$.

Method of Solution

The aforementioned system of governing equations and boundary conditions is solved numerically with the finite element method (FEM). The domain discretization into finite elements needs special attention, as explained in detail in our previous work.[18] Of course any of the sophisticated free-surface methods developed over the years and mentioned in the Introduction can overcome these problems. However, we have found that the easiest way to solve this problem was the method originally used by Mavridis et al.[3] It employed quadratic triangular elements and a polar grid, starting with an initial flow domain, which had a semicircle at the flow front. For this purpose, the original MACVIP program[25] was slightly modified to handle this polar grid arrangement, where now the spines are at a fixed angle ϕ. The new finite element meshes (designated as POLAR-M1 to M3 or for short PM1, PM2, PM3) are shown in Figure 3, and their characteristics are given in Table 1, regarding number of nodes on the free surface, elements, nodes and degrees of freedom (dof). POLAR-M1 is the one used by Mavridis et al.[3] and was used here for early trial runs to check the results and gain experience with the different flow parameters. Its entry length is $2R$, which is quite adequate for Newtonian creeping flows with no other effects present. However, for the other meshes the entry has been set at $-5R$ to accommodate nonlinear phenomena, which need an adequate length to develop (such as convective or compressible flows). The exit is set at 0 for ease of reporting the flow front location. The adequacy of the entry length was also checked at each run by plotting the centerline velocity profile and observing its leveling off in the region near the entry.

The initial mesh configuration was that of a rectangular domain with the exit at 0 plus the extra elements of the polar grid making up a semicircle. After an initial solution was obtained in this fixed domain, the velocities at the free surface were integrated (having subtracted the velocity $V_{B'}$ of the stagnation point B′) according to the formula (e.g., for the axisymmetric case)

$$z_{new} = z_w + \int_R^r \frac{v_z - V_{B'}}{v_r} dr, \tag{15}$$

where z_{new} is the new position of the front, and z_w is the exit position at point C (see Figure 2). The numerical integration was carried out using Simpson's rule.

The newly calculated free surface is used for remeshing. The new change in distance $dz = z_{new} - z_w$ is projected onto the spine to give a new spine radius $r + dr$, according to $dr = dz\sin\phi$. Thus, the spine angle ϕ is always kept constant to avoid distorted meshes. With this method, the results for the free surface were mesh-independent even with few elements, as will be shown later.

The aforementioned method of finding the free surface assumes very viscous fluids where the contact angle is set at

Table 1. Finite Element Mesh Characteristics used in the Simulations and Newtonian Base Results for the Centerline Location of the Flow Front, χ, and the Front Pressure Correction (Exit Correction), n_{ex}; POLAR Corresponds to 6-node Triangular Elements

Mesh	No. of FS Nodes	No. of Elements	No. of Nodes	No. of Dof	χ (Planar)	n_{ex} (Planar)	χ (Axisym)	n_{ex} (Axisym)
POLAR-M1*	29	298	647	1371	0.893	0.0986	0.833	0.1624
POLAR-M2	39	1541	3182	6983	0.895	0.0985	0.835	0.1622
POLAR-M3	77	6202	12603	28005	0.895	0.0985	0.835	0.1622

*Used by Mavridis et al.[3]

Table 2. Range of Simulations for Different Parameters in Fountain Flow of Newtonian Fluids (St^- and St^+ Refer to Gravity Opposing or Aiding the Flow, Respectively)

	Limits of Parameter Range	
Dimensionless Number	Planar	Axisymmetric
Re	[0–6.8]	[0–6]
St^-	[0–40]	[0–40]
St^+	[0–0.59]	[0–0.87]
B	[0–0.12]	[0–0.12]
B_p	[0–0.09]	[0–0.04]
B_{sl}	[0–100]	[0–100]
Ca	[∞–0.02]	[∞–0.11]

180°, and is not further modified by the flow.[3,6] However, the most general physical case involves an arbitrary (in general) contact angle that is actually dynamically modified so as to accommodate a force balance at the contact line. Modifications to account for this more general situation exist in the literature,[12] and some preliminary results have also been published in association with the fountain flow effect recently.[26]

In all the aforementioned cases, the iterative scheme was direct substitution (Picard iterations) with a zero-order continuation in a parameter (Re, St, B, B_p, B_{sl}, Ca). The criteria for termination of the iterative process were for both the norm-of-the-error and the norm-of-the-residuals $<10^{-3}$, and for the maximum free-surface change $<10^{-5}$.

With the polar grid arrangement starting from a semicircle and employing radial spines, we were able to reach extended ranges of the relevant parameters. The number of iterations for the Newtonian creeping incompressible base case was 9 (planar), and 10 (axisymmetric) with an under-relaxation factor $\omega = 0.5$. Convergence for most runs was fast and good for a wide range of parameters as shown in Table 2, except near the limiting values, as will be discussed later.

Results and Discussion

Before we embark on the effect of the different parameters, it is instructive to present the base case of Newtonian creeping results ($Re = St = B = B_p = B_{sl} = 0$, $Ca = \infty$) in some detail, in order to establish their accuracy. The results are given in terms of the dimensionless change in the location of the advancing front χ, and of the dimensionless change in pressure drop over and above the fully developed values n_{ex}. These are defined as follows.

The dimensionless *centerline front location* χ, defined by

$$\chi = \frac{\Delta z_{cl}}{R} \quad \text{or} \quad \chi = \frac{\Delta x_{cl}}{H}, \tag{16}$$

where $\Delta z_{cl} = z_{cl} - z_w$ is the change in the centerline position z_{cl} with respect to wall position z_w (distance BB′, see Figure 2); correspondingly for planar geometries $\Delta x_{cl} = x_{cl} - x_w$.

The dimensionless *front pressure correction* or *exit correction* n_{ex}, defined by

$$n_{ex} = \frac{\Delta P_w - \Delta P_0}{2\tau_w}, \tag{17}$$

where ΔP_w is the overall pressure drop in the system calculated at the wall, ΔP_0 is the pressure drop based on the fully developed flow in the tube (channel) without the fountain flow, and τ_w is the shear stress for fully developed Poiseuille flow at the tube (channel) wall.

The Newtonian base values are: $\chi = 0.895$ (planar), and $\chi = 0.835$ (axisymmetric). We note a difference of 6% in favor of the planar geometry (cf. the extrudate swell values of 18.63% for planar, and 12.65% for axisymmetric geometries).[19,23] Thus, the maximum thrust forward of the advancing front at the centerline can be at most 89.5% (flat channel), and 83.5% (tubes) for Newtonian fluids. As pointed out before,[18] the fountain flow problem is more difficult than the extrudate swell problem, because the free surface is perpendicular to the main flow direction, whereas in extrudate swell the free surface follows the main flow direction. Also, in the Newtonian extrudate swell the domain gets deformed in the order of 13–19%, while in fountain flow the domain is deformed in the order of 84–90%. Starting from a semicircle, the deformations are then reduced to the same order as in the extrudate swell.

The exit correction n_{ex} is obtained from the wall pressure values given by the simulations at the entry of the domain upstream according to Eq. 17. This is a very sensitive quantity and reflects the adequacy of the domain length, the imposed entry profile, and the finite element mesh used. The creeping values are 0.099 (planar) and 0.162 (axisymmetric). The corresponding values from the extrudate swell problem are 0.147 (planar) and 0.227 (axisymmetric).[19]

Inertial flows—effect of Re

The calculations are pursued for increasing Reynolds numbers, in both planar ($0 \le Re \le 6.8$), and axisymmetric ($0 \le Re \le 6$) geometries. Convergence was good and fast up to $Re = 6$ (planar), and $Re = 5$ (axisymmetric) with under-relaxation $\omega = 0.5$. After that, convergence became increasingly difficult, and at the limit more than 100 iterations were needed with $\omega = 0.1$. The results are rather dramatic compared with the creeping limit as shown in Figure 4, where symbols are put here and in the following graphs to show the parameter-continuation steps. Inertia increases the χ–values, reaching for $Re = 6$, $\chi = 2.24$ (planar), and $\chi = 2.43$ (axisymmetric). At $Re = 3.5$, planar and axisymmetric flows have the same $\chi = 1.43$. Below that value, the planar geometry has the more advanced front, and the opposite is true beyond the cross-over point. The domain length does not play a role in the results, since a longer domain ($-5R$) gave the same results as a shorter one ($-2R$). This is not surprising due to the simple shear flow, which is prevalent almost up to the exit of the channel.

Figure 5a shows a comparison of the present results for the free surface for different Re numbers for the planar geometry (drawn in scale). The semicircle is reached at $Re \approx 1$. However, all the interesting results appear after that, when increasing inertia leads to a dramatic increase in the shape of the flow front. This is in contrast to accepted knowledge that the flow front is basically a semicircle for all cases. The flow front thrusts forward as the Re number increases. The profiles are reminiscent of the transient Poiseuille flow, but the present ones are obtained from a steady-state solution

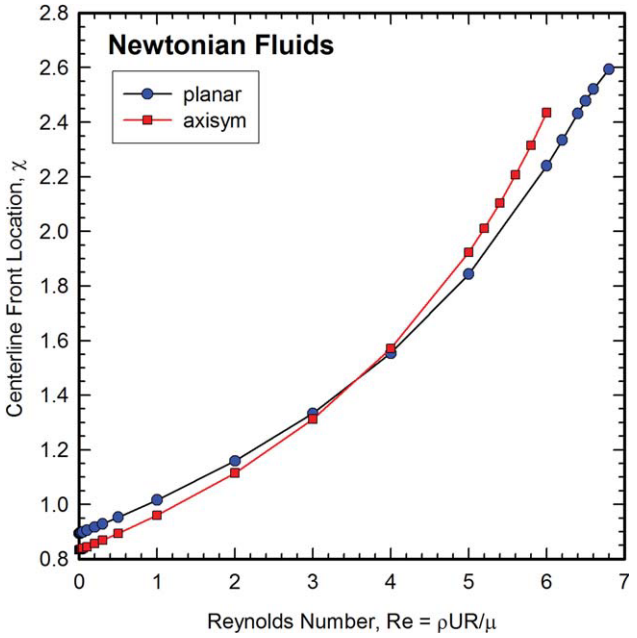

Figure 4. Dimensionless centerline front location χ as a function of the Reynolds number *Re*.

Symbols are put here and in the following to show the parameter-continuation steps. [Color figure can be viewed in the online issue, which is available at www.interscience.wiley.com.]

and are solely due to the effect of inertia. The pronounced forward thrust was also found for pseudoplastic and viscoplastic fluids,[18] but the profiles are markedly different. In the former case the forward thrust was also evident in the upper part of the profile after the die wall, where the fluid wanted to continue moving at the same level as the wall, and then bended precipitously toward the centerline. This is not the case in the inertial profiles, which keep their parabolic-like behavior for all *Re* numbers. The extended profiles for the higher *Re* are the main reason for losing convergence above a limiting *Re* value, and making this a difficult problem to solve.

The corresponding results for the axisymmetric case are shown in Figure 5b. The trends are similar to the planar case. We observe again that for $Re < 3.5$, the planar results are higher, but above that the reverse is true for the axisymmetric ones.

The results for the exit correction n_{ex} are presented in Figure 6. The effect of inertia is to decrease the n_{ex} values monotonically and substantially when moving away from the inertialess behavior. At $Re \approx 2$, the planar flows show no extra pressure losses, after which inertia creates a subpressure in the field. The same occurs for axisymmetric flows at $Re \approx 2.7$.

Gravity flows—effect of St

The calculations are then pursued for gravity flows, both when gravity opposes the flow (St^-), and when it acts with the flow (St^+). The former case was studied in the work by Coyle et al.[4] who showed that gravity drastically reduces the flow front, reaching values as low as $\chi \approx 0.28$ for $St^- \approx 33$.

The results for the centerline front location (χ) as a function of the Stokes number St^- are given in Figure 7 for the two geometries. There is a monotonic exponential decrease for both cases, where χ reaches low values for relatively high St^- numbers. The axisymmetric case exhibits smaller

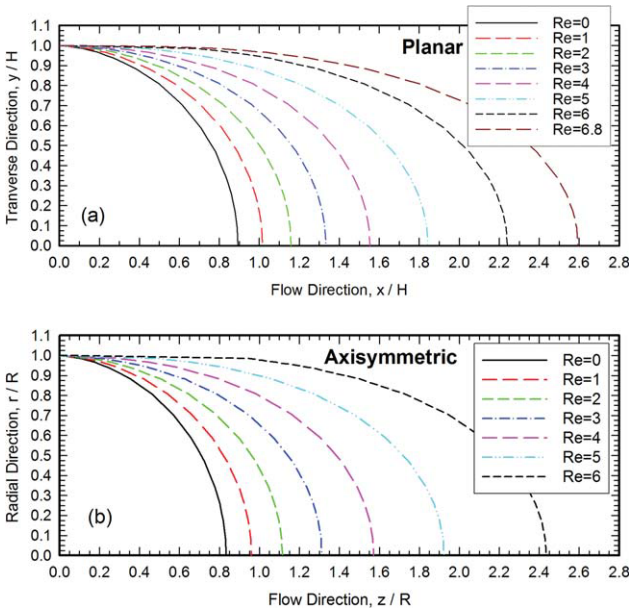

Figure 5. Comparison of advancing front shapes for different Reynolds numbers *Re*: (a) planar flow, and (b) axisymmetric flow.

[Color figure can be viewed in the online issue, which is available at www.interscience.wiley.com.]

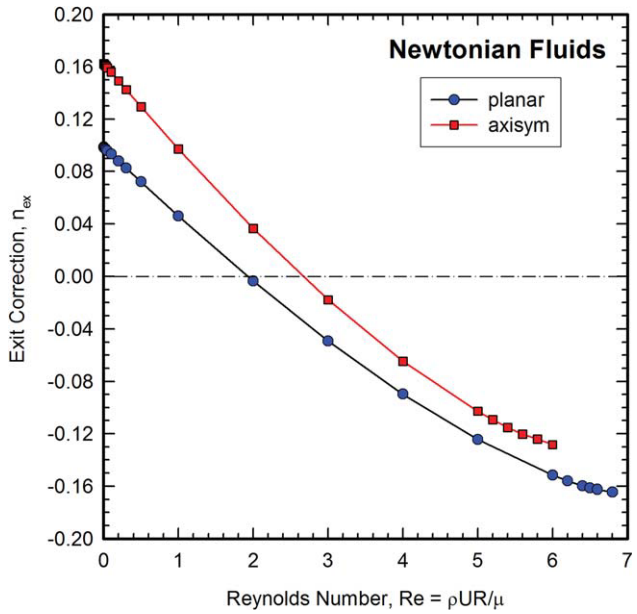

Figure 6. Dimensionless front pressure correction (exit correction) n_{ex} as a function of the Reynolds number *Re*.

[Color figure can be viewed in the online issue, which is available at www.interscience.wiley.com.]

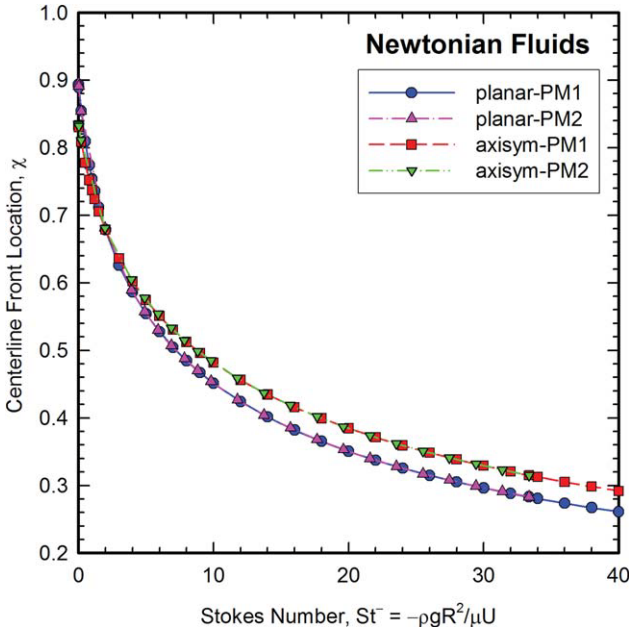

Figure 7. Dimensionless centerline front location χ as a function of the Stokes number St^- when gravity opposes the flow.

Results from polar meshes of Figure 3 showing mesh-independence. [Color figure can be viewed in the online issue, which is available at www.interscience.wiley.com.]

values up to $St^- = 2$, where both cases give the same $\chi \approx 1.68$. After that, the planar values are somewhat lower that the axisymmetric ones for the same St^-. Results obtained with polar meshes PM1 and PM2 showed no visible difference for the whole range of simulations, as evidenced in Figure 7. The domain length has no effect on the χ values. Convergence for the whole range of simulations was good and fast. Around 10 iterations were used for St^- up to 6 with under-relaxation $\omega = 0.5$. After that, less than 20 iterations were needed with $\omega = 0.2$. The runs were terminated at $St^- = 40$ due to lack of interest.

Figure 8a shows a comparison of these results for the free surface for different St^- numbers for the planar geometry. The flow front rapidly loses its curvature as St^- increases. The results of Coyle et al.[4] were easily reproduced for $St^- = 33.354$ (without surface tension effects, which as will be shown later adds little to the curvature for $Ca = 5$, the experimental value of Ca). The corresponding results for the axisymmetric case are similar, as shown in Figure 8b.

The results for the exit correction n_{ex} as a function of the Stokes number St^- are given in Figure 9 for the two geometries. The exit correction rises linearly for both cases. A linear regression gave the following values for n_{ex} as a function of St^-

$$n_{ex} = aSt^- + b, \tag{18}$$

where $(a, b) = (0.372, 0.099)$ for the planar, and $(a, b) = (0.275, 0.162)$ for the axisymmetric geometry. The regression $R^2 = 0.9996$ (planar), and 0.9998 (axisymmetric).

The situation is radically different when gravity acts in the direction of flow. The flow front rapidly increases with St^+, and convergence is easily lost for $St^+ = 0.6$ (planar) and $St^+ = 0.88$ (axisymmetric). The results for the centerline front location (χ) as a function of the Stokes number St^+ are given in Figure 10 for the two geometries. The planar results are always higher than the axisymmetric ones. The semicircle is reached for $St^+ = 0.35$ (planar), and $St^+ = 0.70$ (axisymmetric). It is observed that the increase of χ near the limiting values is exponential, and this leads to an abrupt loss of convergence. It is quite conceivable that these *limit*

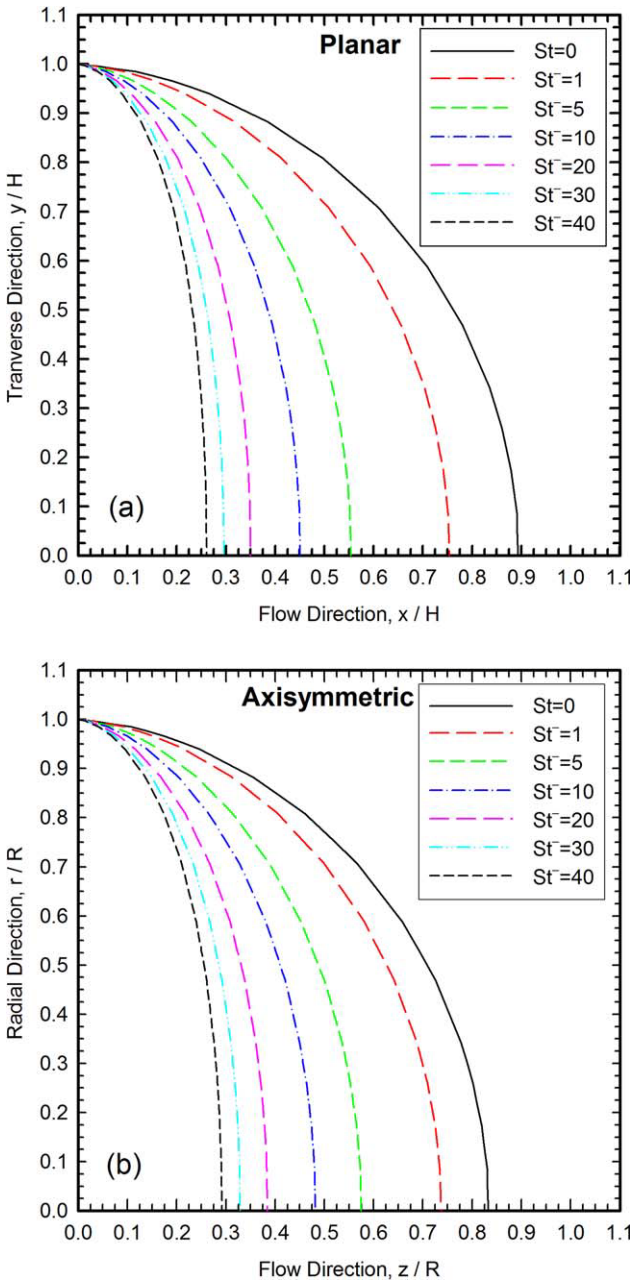

Figure 8. Comparison of advancing front shapes for different Stokes numbers St^- when gravity opposes the flow: (a) planar flow, and (b) axisymmetric flow.

[Color figure can be viewed in the online issue, which is available at www.interscience.wiley.com.]

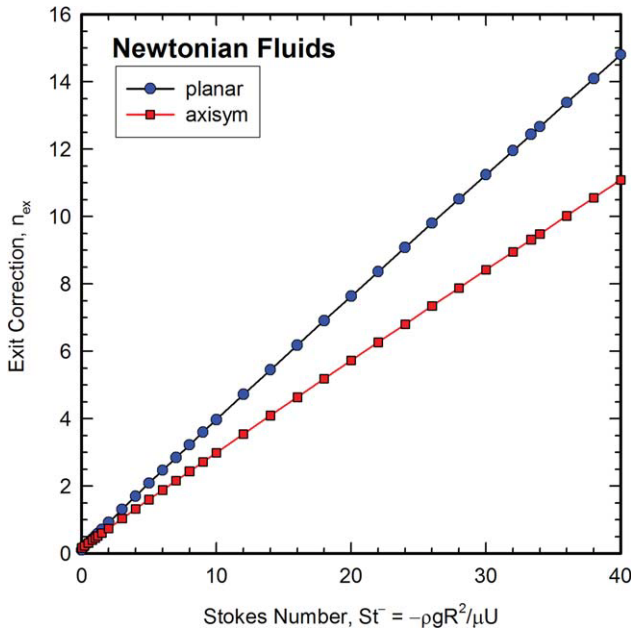

Figure 9. Dimensionless exit correction n_{ex} as a function of the Stokes number St^- when gravity opposes the flow.

[Color figure can be viewed in the online issue, which is available at www.interscience.wiley.com.]

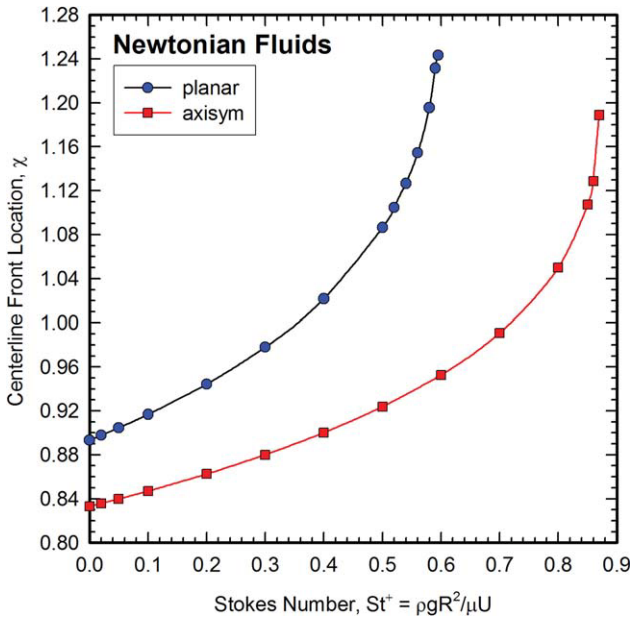

Figure 10. Dimensionless centerline front location χ as a function of the Stokes number St^+ when gravity aids the flow.

[Color figure can be viewed in the online issue, which is available at www.interscience.wiley.com.]

points are real in the parameter space studied, as they were observed with all meshes used, and can be related to an onset of instabilities. However, this is best pursued with a stability analysis based on the Jacobian entries of a Newton-Raphson scheme, something which is not done here.

Figure 11a shows a comparison of these results for the free surface for different St^+ numbers for the planar geometry (in scale). The flow front rapidly increases its curvature as St^+ increases. The corresponding results for the axisymmetric case are similar as shown in Figure 11b. They are always lower than the planar ones for the same St^+ number.

The results for the exit correction n_{ex} as a function of the Stokes number St^+ are given in Figure 12 for the two geometries. The exit correction drops linearly for both cases. A linear regression gave the following values for n_{ex} as a function of St^+

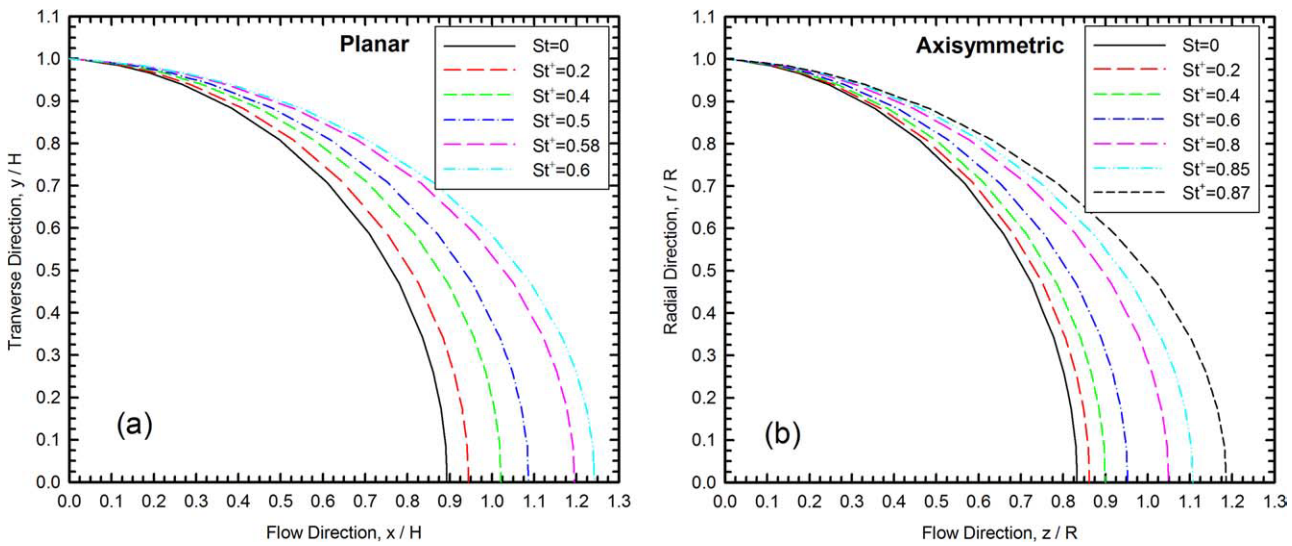

Figure 11. Comparison of advancing front shapes for different Stokes numbers St^+ when gravity aids the flow: (a) planar flow, and (b) axisymmetric flow.

[Color figure can be viewed in the online issue, which is available at www.interscience.wiley.com.]

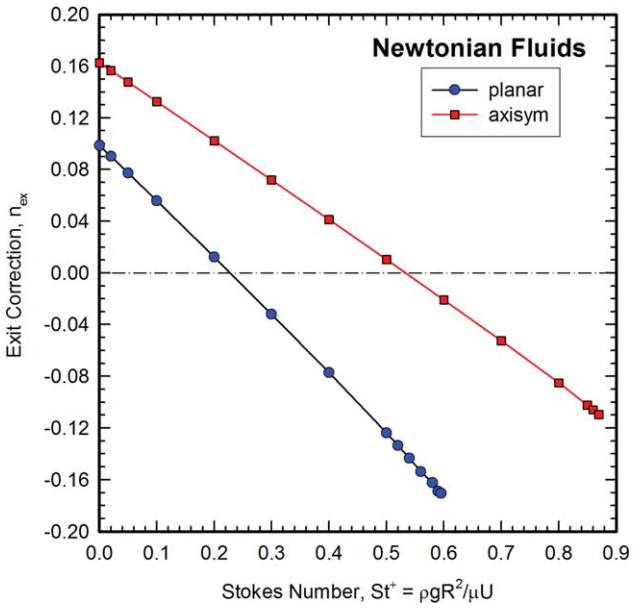

Figure 12. Dimensionless exit correction n_{ex} as a function of the Stokes number St^+ when gravity aids the flow.

[Color figure can be viewed in the online issue, which is available at www.interscience.wiley.com.]

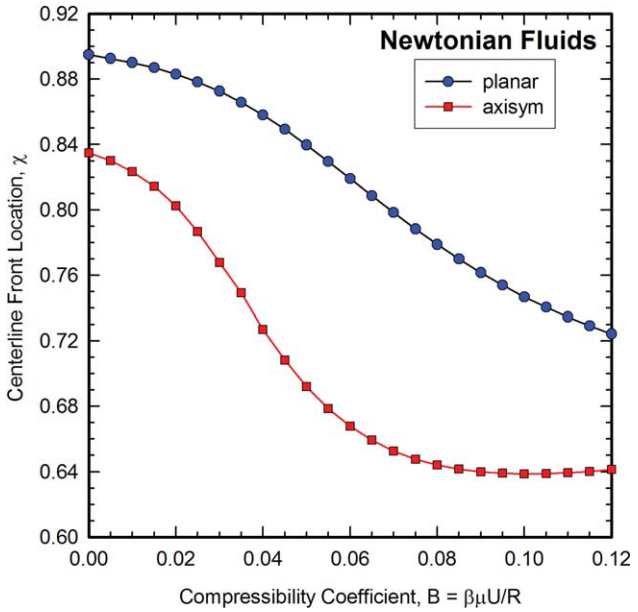

Figure 13. Dimensionless centerline front location χ as a function of the compressibility coefficient B.

[Color figure can be viewed in the online issue, which is available at www.interscience.wiley.com.]

$$n_{ex} = aSt^+ + b, \tag{19}$$

where $(a, b) = (-0.447, 0.099)$ for the planar, and $(a, b) = (-0.309, 0.162)$ for the axisymmetric geometry. The regression $R^2 = 0.9995$ (planar), and 0.9997 (axisymmetric).

Compressible flows—effect of B

The calculations are then pursued for compressible flows. To our knowledge no such studies are to be found in the literature, even though under high-pressures exerted in injection molding (they can exceed 100 MPa and perhaps reach 200 MPa),[2] compressibility cannot be ignored. It should be noted that compressibility has been included in extrudate swell studies.[19,22,27,28]

The compressible flow field depends on the domain length, and the results shown here have been produced with a length of $2R$. The results for the centerline front location χ as a function of the compressibility coefficient B are given in Figure 13 for the two geometries. There is a monotonic sigmoid decrease for both cases, where χ reaches low-values for relatively high B numbers. The axisymmetric case exhibits always markedly lower values than the planar one for the whole range of $0 \leq B \leq 0.12$. Except for the lower values of B (≤ 0.02), convergence was slow and difficult. For example for the highest value of $B = 0.12$, and starting from the solution at $B = 0.115$, around 2,500 iterations were needed with severe under-relaxation $\omega = 0.002$. Similar difficult convergence behavior was also found in our recent work with power-law and Bingham fluids.[18]

Figure 14 shows a comparison of these results for the free surface for different B numbers for the planar geometry (in scale). The flow front loses its curvature as B increases, but this loss is less pronounced than in the opposing-gravity flow (effect of St^-). The corresponding results for the axisymmetric case are similar but always smaller, and are not shown here.

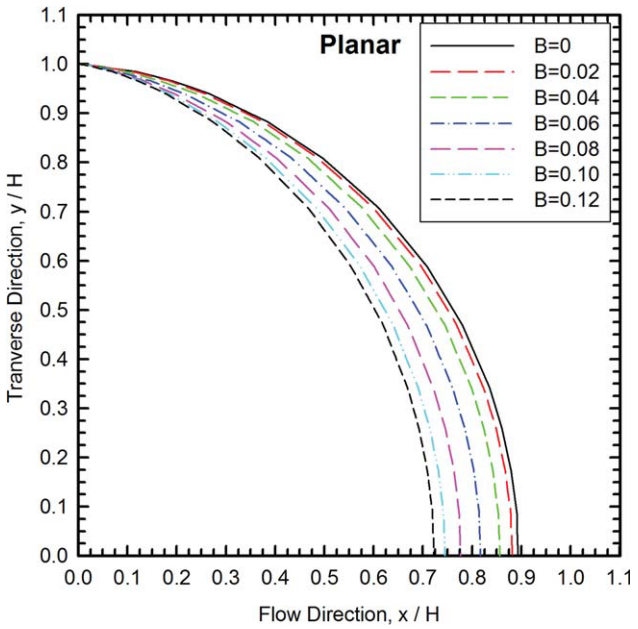

Figure 14. Comparison of advancing front shapes for different compressibility coefficients B (planar flow).

[Color figure can be viewed in the online issue, which is available at www.interscience.wiley.com.]

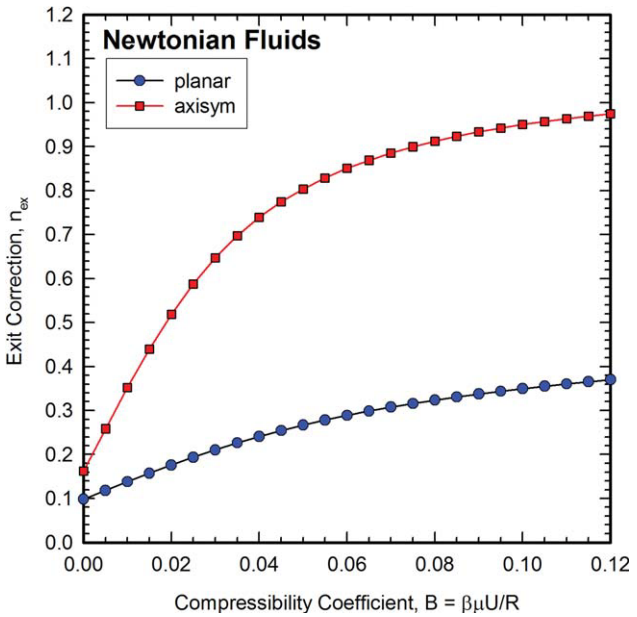

Figure 15. Dimensionless exit correction n_{ex} as a function of the compressibility coefficient B.

[Color figure can be viewed in the online issue, which is available at www.interscience.wiley.com.]

The results for the exit correction n_{ex} as a function of B are given in Figure 15 for the two geometries. The exit correction rises quadratically for both cases. A regression analysis gave the following cubic polynomial for n_{ex} as a function of B

$$n_{ex} = aB^3 + bB^2 + cB + d, \tag{20}$$

where $(a, b, c, d) = (46.312, -23.365, 4.391, 0.099)$ for the planar, and $(a, b, c, d) = (741.1, -212.17, 21.623, 0.162)$ for the axisymmetric geometry. The regression $R^2 = 0.9998$ (planar), and 0.9996 (axisymmetric).

Pressure-dependence of viscosity—effect of B_p

The calculations are then pursued for flows with a pressure-dependent viscosity. This case has been studied before,[20] realizing the fact that under high-pressures exerted in injection molding, the pressure effect on the viscosity cannot be ignored.[21]

As with compressible flows, the results depend on the domain length. Those shown here have been produced with a length of $2R$, as was done by Huilgol and You.[20] The inlet Poiseuille velocity profile is set as the parabolic one for a unit mean velocity. The results for the centerline front location χ as a function of the pressure-shift coefficient B_p are given in Figure 16 for the two geometries. There is a linear increase for both cases, at least in the range of B_p-numbers. The axisymmetric case exhibits always markedly lower values than the planar one for the range of simulations. Due to the exponential nature of the pressure-dependence of the viscosity (Eq. 5), convergence was lost suddenly at low-values of B_p ($B_p = 0.09$ for the planar and $B_p = 0.041$ for the axisymmetric case). As was the case with gravity aiding the flow, it is quite conceivable that these *limit points* are real in the parameter space studied, and can be related to an onset of instabilities. Up to those B_p-limiting values, convergence was good and fast (four iterations were sufficient for most of the runs). The same range of B_p values and results for χ for the planar case were obtained by Huilgol and You[20] (their β-parameter is the reciprocal of our β_p or B_p), and they cover the range of all practical situations in injection molding.

The results for the exit correction n_{ex} as a function of B_p are given in Figure 17 for the two geometries. It should be mentioned that the values of ΔP_0 and τ_w appearing in Eq. 17 are those for fully developed Poiseuille flow with no pressure-dependence of the viscosity. The exit correction rises exponentially for both cases, with the axisymmetric case rising much faster for the same B_p-number.

We now turn our attention to the effect of dimensionless parameters as they arise from the flow along or across the domain boundaries. These include the effect of slip at the solid channel or tube walls (hence, the effect of slip parameter B_{sl}), and the effect of surface tension (hence, capillary number, Ca) on the flow front.

Flows with slip at the wall—effect of B_{sl}

The calculations are then pursued for flows with slip at the wall. This case has been studied in a limited range before,[29] and showed that slip reduces somewhat the flow front and substantially the pressure drop in the system. Here a thorough well-documented range of simulations is undertaken as was done in our previous studies for the problem of extrudate swell.[22]

The simulations have been pursued for a wide range of B_{sl}-values from 0 (no slip) to 100 (approaching perfect slip

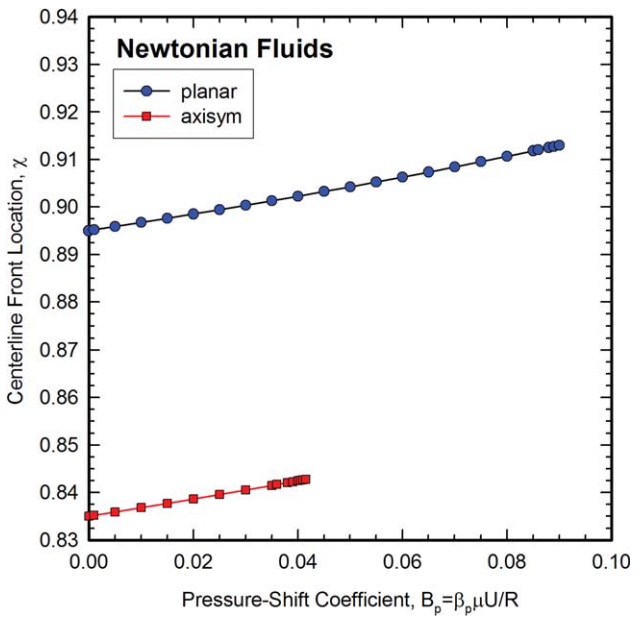

Figure 16. Dimensionless centerline front location χ as a function of the pressure-shift coefficient B_p.

[Color figure can be viewed in the online issue, which is available at www.interscience.wiley.com.]

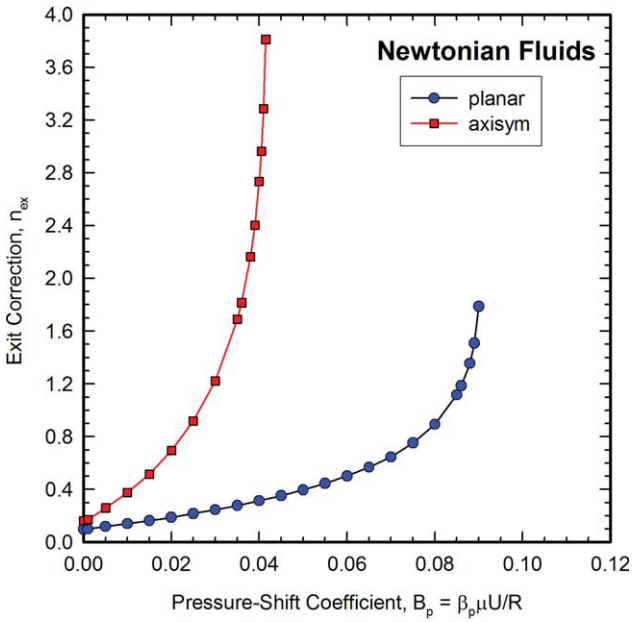

Figure 17. Dimensionless exit correction n_{ex} as a function of the pressure-shift coefficient B_p.

[Color figure can be viewed in the online issue, which is available at www.interscience.wiley.com.]

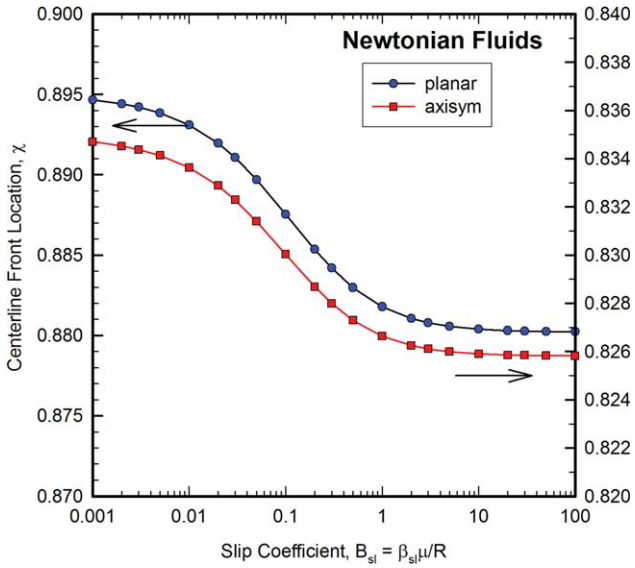

Figure 18. Dimensionless centerline front location χ as a function of the slip coefficient B_{sl}.

[Color figure can be viewed in the online issue, which is available at www.interscience.wiley.com.]

for which $B_{sl} \to \infty$). Convergence for this problem was always good and fast, requiring at most 11 iterations in the middle range of B_{sl}-values where the changes were bigger. The under-relaxation parameter was always kept at $\omega = 0.5$. The results do not depend on the domain length, as evidenced by trial runs with die lengths of either $2R$ or $5R$. Again, this is not surprising due to the simple-shear nature of the flow almost up to the channel exit.

The results for the centerline front location χ as a function of the slip coefficient B_{sl} are given in Figure 18 for the two geometries. There is a typical sigmoid decrease for both cases in the range of B_{sl}-values. This typical behavior has been also observed in the extrudate swell problem.[22] Most of the changes occur in the range $0.01 < B_{sl} < 1$. However, these changes are not dramatic (from 0.895 to 0.88, less than 2%). The axisymmetric case exhibits always markedly lower values than the planar one for the whole range of simulations (hence, the change of scale on the right axis). As B_{sl} increases approaching perfect slip ($B_{sl} \to \infty$), the flow front reaches a constant value for χ, which is $\chi \approx 0.88$ for planar, and $\chi \approx 0.826$ for axisymmetric geometry. This is in sharp contrast with the problem of extrudate swell, where there the free surface tends to go to zero swell, due to a plug velocity profile everywhere in the flow field.

The results for the exit correction n_{ex} as a function of B_{sl} are given in Figure 19 for the two geometries. It should be mentioned that the values of ΔP_0 and τ_w appearing in Eq. 17 are those for fully developed Poiseuille flow with slip according to the analytical solutions based on a linear slip law.[19,22] The exit correction follows the sigmoid behavior of the flow front for both cases, with the axisymmetric case giving always higher values for the same B_{sl}-number. Eventually all values go to 0, as the fluid slips perfectly along the solid walls. Therefore, slip in fountain flow has a small effect on the flow front, while it reduces substantially the excess pressure losses in the system.

Flows with surface tension—effect of Ca

The calculations are then pursued for fluids having non-negligible surface tension. This case has been studied before in a single run,[4] but the influence of surface tension was coupled with gravity, and, therefore, its effect was not clear.

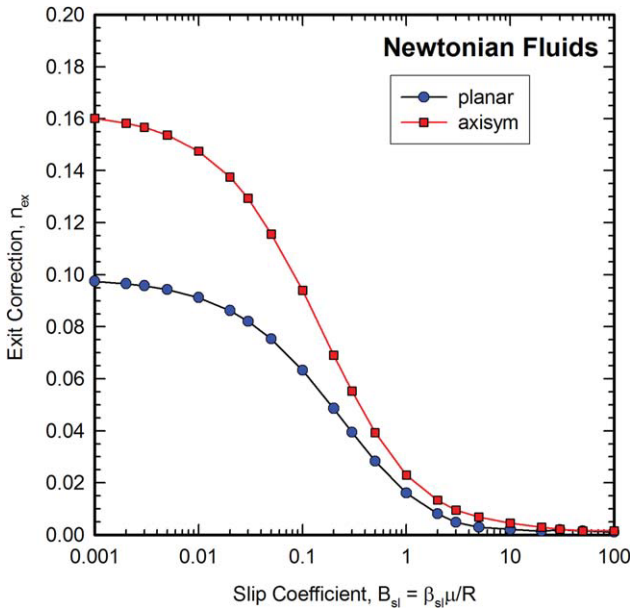

Figure 19. Dimensionless exit correction n_{ex} as a function of the slip coefficient B_{sl}.

[Color figure can be viewed in the online issue, which is available at www.interscience.wiley.com.]

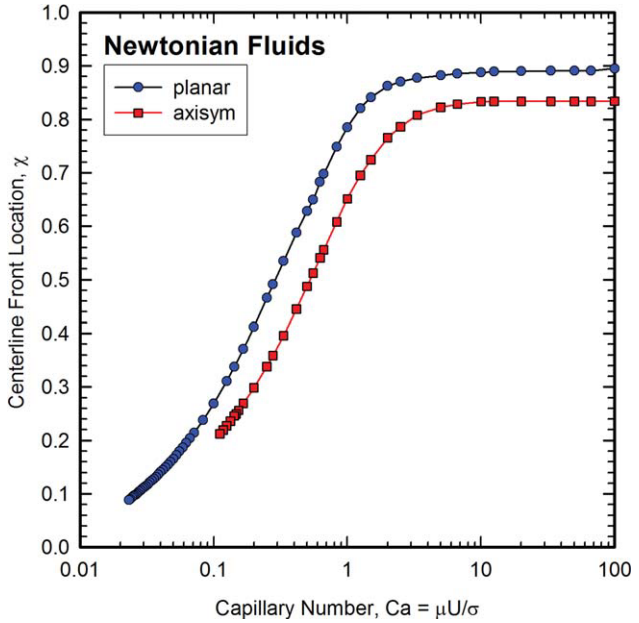

Figure 20. Dimensionless centerline front location χ as a function of the capillary number *Ca*.

[Color figure can be viewed in the online issue, which is available at www.interscience.wiley.com.]

Here a thorough well-documented range of simulations is undertaken as was done in previous studies for the problem of extrudate swell.[23,24] As was the case with slip, the results do not depend on the domain length, as evidenced by trial runs with die lengths of either $2R$ or $5R$. The same arguments hold as before for this behavior. Another point to notice is the assumption of a constant contact angle of 180°, which does not further change with the flow, as noted earlier.

The simulations have been pursued for a wide range of Ca values from ∞ (or a big number, say 10,000) (no surface tension) to 0.02 (strong surface tension effects). Convergence for this problem was good and relatively fast, requiring usually around 10–30 iterations, except when approaching the limiting Ca value where many more iterations were needed, and eventually divergence occurred at low values of Ca ($Ca = 0.023$ for the planar and $Ca = 0.11$ for the axisymmetric case). The under-relaxation parameter was always kept at $\omega = 0.5$.

The results for the centerline front location χ as a function of the capillary number Ca are given in Figure 20 for the two geometries. There is a typical sigmoid decrease for both cases in the range of Ca-values. This typical behavior has been also observed in the extrudate swell problem.[23] The axisymmetric case exhibits always markedly lower values than the planar one for the whole range of simulations. As Ca decreases approaching zero (strong surface tension effects, $Ca \to 0$), the flow front seems to want to approach a zero value for χ, corresponding to a flat front. This is also the case with the problem of extrudate swell, where the free surface tends to go to zero swell, due to strong surface tension, which does not allow the fluid to swell.[23] The results for the flow front and for different Ca numbers resemble very much the ones of Figure 8 for different St^- numbers, and they are not given here. It is interesting to note that the results of Coyle et al.[4] corresponding to $Ca = 5$ have a very small influence on the flow front compared with the no surface tension case, as also evidenced in Figure 20 (changes of about 1%).

The results for the exit correction n_{ex} as a function of Ca are given in Figure 21 for the two geometries. The exit correction follows the sigmoid behavior of the flow front location for both cases, with the axisymmetric case giving higher values for the same Ca-number in the high range of Ca, while the opposite is true for at low values of Ca. The cross-over point where the two corrections are equal is at $Ca = 1.2$. At about $Ca \approx 0.5$ (planar), the exit correction goes to 0, after which there is a negative excess pressure loss in the system (subpressure) due to the strong surface tension effects at the flow front. The same occurs for $Ca \approx 0.8$ for the axisymmetric geometry.

Flow fields

It is instructive to show sample flow fields of the major variables for the various fluid mechanics parameters studied earlier. This is done in the form of contours in Figures 22 and 23 for the magnitude of the velocity vector $|u| = \sqrt{u_r^2 + u_z^2}$ = UBAR, the pressure P (isobars), and the magnitude of the extra stress tensor $|\tau| = \sqrt{\frac{1}{2}\left(\overline{\overline{\tau}} : \overline{\overline{\tau}}\right)}$ = TBAR. The axisymmetric case is chosen as more demanding, and the graphs are drawn in scale for easy comparisons. In each parameter case, the limiting value is chosen for depiction, just before divergence occurred or the runs were stopped. The comparisons are made with the base case of ($Re = St = B = B_p = B_{sl} = 0$, $Ca = \infty$), which is given in the first row of Figure 22. In this Figure are given the cases of St^-, B, B_p, B_{sl}, and Ca, for which the flow front is around

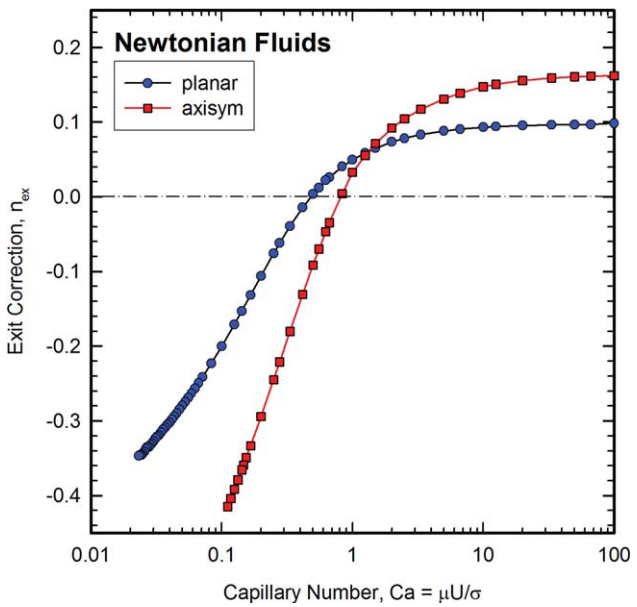

Figure 21. Dimensionless exit correction n_{ex} as a function of the capillary number *Ca*.

[Color figure can be viewed in the online issue, which is available at www.interscience.wiley.com.]

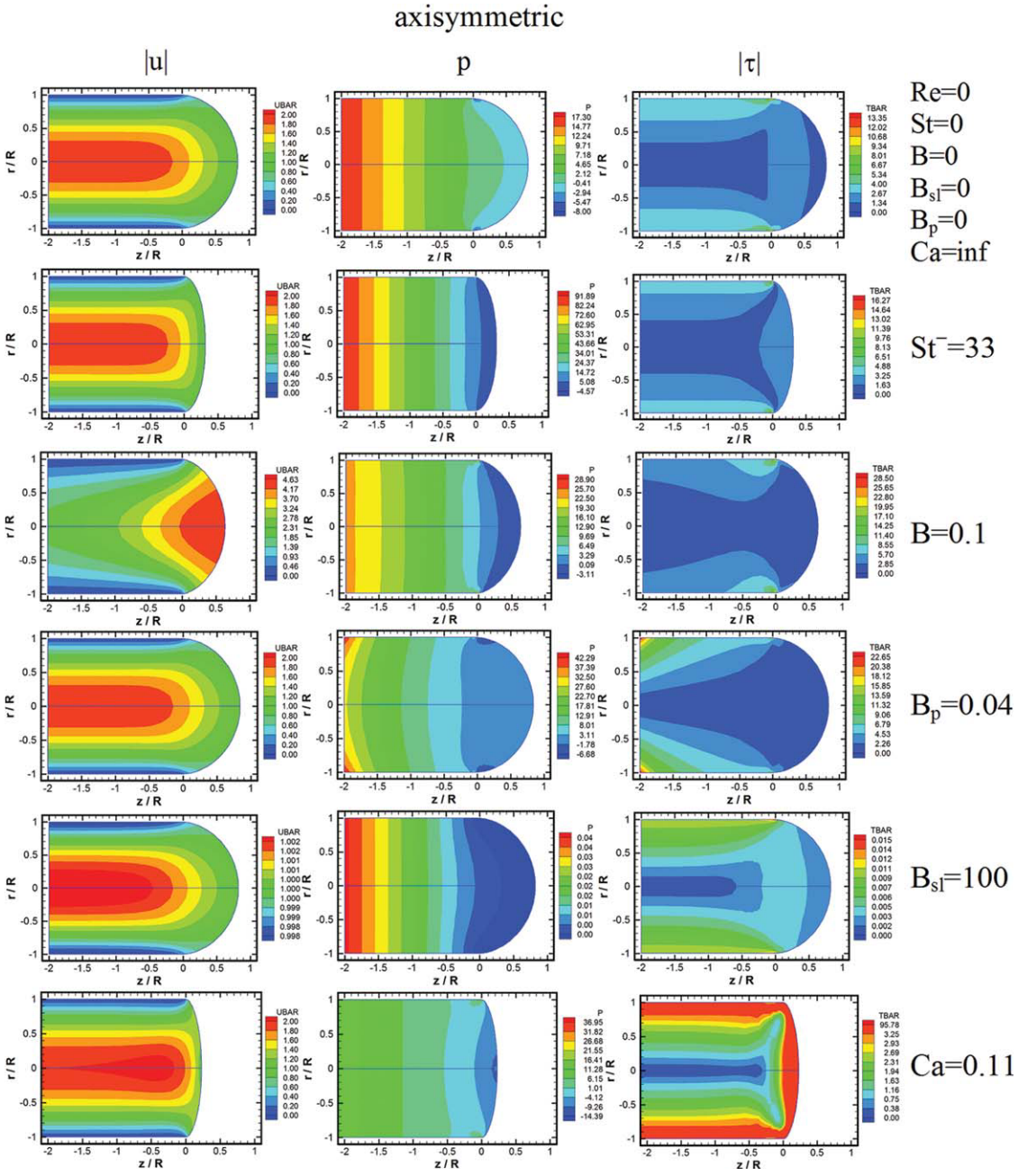

Figure 22. Contour variables for axisymmetric fountain flow of Newtonian fluids: left column, $|\mathbf{u}| = \sqrt{u_r^2 + u_z^2}$ = UBAR, middle column, pressure P, right column $|\tau| = \sqrt{\frac{1}{2}(\bar{\bar{\tau}} : \bar{\bar{\tau}})}$ = TBAR.

The maximum values correspond to the highest number in the legend (red). The minimum values correspond to the lowest number in the legend (blue). Each row represents the parameter effect shown on the right, which is near the limiting value of the parameter range used in the simulations. The graphs are drawn to scale for easy comparisons with the base case (first row). [Color figure can be viewed in the online issue, which is available at www.interscience.wiley.com.]

the semicircle or lower. The cases of Re and St^+, which exceed the semicircle, are given in Figure 23.

A detailed study of the contours for each case reveals interesting trends, which are not always anticipated. So we see that gravity opposing the flow (effect of St^-, second row of Figure 22) reduces the flow front substantially, as was also found by Coyle et al.[4] for the same St number, but apart from that the flow field does not show any surprises. Compressibility (effect of B, third row of Figure 22) accelerates the flow toward the flow front. A pressure-dependent viscosity (effect of B_p, fourth row of Figure 22) bends the isobars and influences the stresses, but not the velocity contours. Slip at the wall (effect of B_{sl}, fifth row of Figure 22) reduces drastically the changes in the velocity field (almost plug flow, with velocity values around 1), while the pressure and stress values become very small. Surface tension (effect of

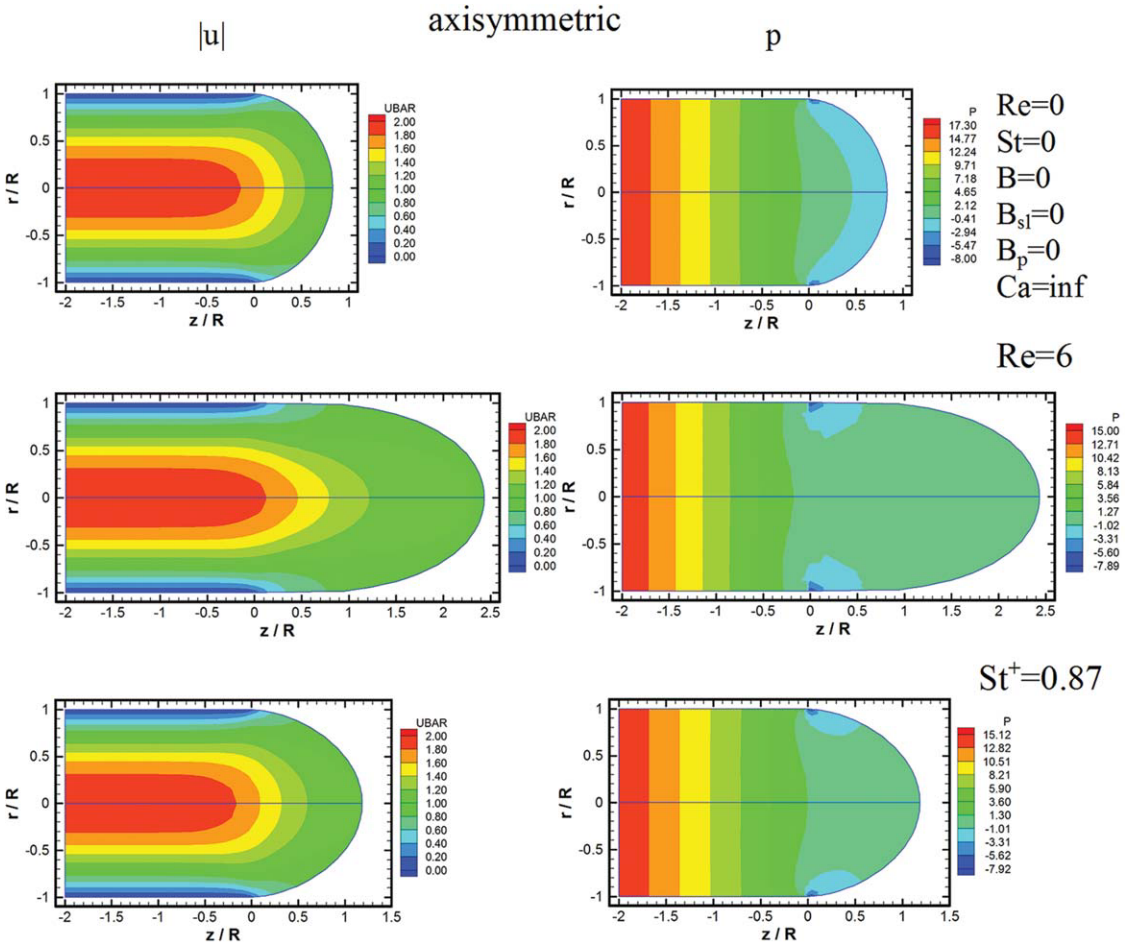

Figure 23. Contour variables for axisymmetric fountain flow of Newtonian fluids: left column $|\mathbf{u}| = \sqrt{u_r^2 + u_z^2}$ = UBAR, right column, pressure P.

The maximum values correspond to the highest number in the legend (red). The minimum values correspond to the lowest number in the legend (blue). Each row represents the parameter effect shown on the right, which is near the limiting value of the parameter range used in the simulations. The graphs are drawn to scale for easy comparisons with the base case (first row). [Color figure can be viewed in the online issue, which is available at www.interscience.wiley.com.]

Ca, sixth row of Figure 22) shows acceleration toward the flow front, where the stresses are very high at the front, reducing drastically its curvature.

The results of Figure 23 show the drastic increase of the flow front when inertia is present (effect of *Re*, second row of Figure 23). The flow front becomes extended and oval but the changes of the primary variables there (velocities and pressure) are not very big. Gravity aiding the flow (effect of St^+, third row of Figure 23) also extends the flow front, but less so than inertia. Apart from that the flow field does not show any surprises, resembling the base case (first row of Figure 23).

Conclusions

The finite element method has been used to derive numerical solutions for the dimensionless centerline front location and pressure exit correction in fountain flow of Newtonian fluids for planar and axisymmetric domains. Polar grids at the flow front were used for a better representation of the flow field, and the initial guess of a semicircle is crucial to get accurate solutions.

Despite accepted knowledge that the flow front is close to a semicircle for all types of fluids, this is not the case when different forces are at play. Inertia elongates rapidly the flow front as *Re* increases, and it reduces the exit correction. Gravity forces opposing the flow rapidly reduce the flow front as St^- increases, while increasing the exit correction. When gravity forces act in the flow direction, the flow front increases rapidly for relatively small values of St^+, while the exit correction decreases linearly. Compressibility serves to reduce the flow front and increase the exit correction. An exponentially pressure-dependent viscosity serves to increase the flow front linearly and the exit correction exponentially.

Boundary effects include slip at the wall and surface tension at the free surface. As the slip coefficient B_{sl} increases, both the flow front and the exit correction decrease in a sigmoid fashion. However, the effect on slip on the free surface is small (<2%), while the exit correction goes to 0 as slip

becomes dominant. The sigmoid behavior is also evident as Ca decreases (strong surface tension effects), when both the flow front and the exit correction decrease.

Although these results are limited to Newtonian fluids and to a constant contact angle of 180°, their effect should be similar for all fluids, where a combination of variables leads to nonzero dimensionless fluid-mechanics parameters, such as the ones given here. It may be argued that these results do not apply to typical polymer melts used in injection molding. However, a variety of fluids undergo fountain flow under a wide range of conditions, so these results should be of interest to the practitioners in the field of fluid mechanics.

Acknowledgments

The author is indebted to NTUA for travel funding related to this project.

Notation

a = constant in regression model
b = constant in regression model
c = constant in regression model
d = constant in regression model
g = acceleration of gravity, m/s^2
h = free surface location, m
H = half gap, m
$\bar{\bar{I}}$ = identity tensor, dimensionless
L = channel (tube) length, m
$\bar{n}$ = outward normal unit vector, dimensionless
p = pressure, Pa
r = radial coordinate, local radius, m
R = radius, m
R_c = mean curvature of free surface, m
$\bar{t}$ = tangential unit vector, dimensionless
$\bar{u}$ = velocity vector, m/s
U = average velocity, m/s
$V_B{}'$ = stagnation velocity, m/s
v_r = radial velocity, m/s
v_z = axial velocity, m/s
x = axial coordinate, m
y = transverse coordinate, m
z = axial coordinate, m
z_{new} = new position of flow front, m
z_w = position of wall exit, m

Greek letters

β = compressibility coefficient, Pa^{-1}
β_{sl} = slip coefficient, m/Pa·s
β_p = pressure-shift coefficient, Pa^{-1}
γ = surface tension, Pa/m
ΔP_w = wall pressure drop, Pa
Δx_{cl} = axial distance from the channel exit, m
Δz_{cl} = axial distance from the tube exit, m
μ = viscosity, Pa·s
ρ = density, kg/m^3
$\bar{\bar{\sigma}}$ = total stress tensor, Pa
$\bar{\bar{\tau}}$ = extra stress tensor, Pa
τ_w = shear stress, Pa
ϕ = spine angle, deg
χ = centerline position, dimensionless

Subscripts

B' = stagnation point
c = curvature
cl = centerline
ex = exit
new = new position
p = pressure
r = radial
sl = slip
w = wall
z = axial
0 = reference

Dimensionless numbers

$B = \beta UR/\mu$ = compressibility coefficient
$B_p = \beta_p UR/\mu$ = pressure-shift coefficient
$B_{sl} = \beta_{sl}\mu/R$ = slip coefficient
$Ca = \mu U/\gamma$ = capillary number
$n_{ex} = (\Delta P_w - \Delta P_0)/2\tau_w$ = exit correction (front pressure correction)
$Re = \rho UR/\mu$ = Reynolds number
$St = \rho g R^2/\mu U$ = Stokes number

Literature Cited

1. Rose W. Fluid-Fluid Interfaces in Steady Motion. *Nature* 1961; 191:242–243.
2. Tadmor Z, Gogos CG. *Principles of Polymer Processing*. SPE Monograph Series, Wiley, New York; 1979.
3. Mavridis H, Hrymak AN, Vlachopoulos J. Finite element simulation of fountain flow in injection molding. *Polym Eng Sci*. 1986;26:449–454.
4. Coyle DJ, Blake JW, Macosko CW. The kinematics of fountain flow in mold-filling. *AIChE J*. 1987;33:1168–1177.
5. Behrens RA, Crochet MJ, Denson CD, Metzner AB. Transient free-surface flows: motion of a fluid advancing in a tube. *AIChE J*. 1987;33:1178–1186.
6. Mavridis H, Hrymak AN, Vlachopoulos J. Transient free-surface flows in injection mold filling. *AIChE J*. 1988;34:403–410.
7. Beris AN. Fluid elements deformation behind an advancing flow Front. *J. Rheol*. 1987;31:121–124.
8. Schmidt LR. A special mold and tracer technique for studying shear and extensional flows in a mold cavity during injection molding. *Polym Eng Sci*. 1974;14:797–800.
9. Bogaerds ACB, Hulsen MA, Peters GWM, Baaijens FPT. Stability analysis of injection molding flows. *J Rheol*. 2004;48:765–785.
10. Verbeeten WMH, Peters GWM, Baaijens FPT. Differential constitutive equations for polymer melts: The extended pom-pom model. *J Rheol*. 2001;45:823–844.
11. Nickell RE, Tanner RI, Caswell B. The solution of viscous incompressible jet and free-surface flows using finite-element methods. *J Fluid Mech*. 1974;65:189–206.
12. Kistler SF, Scriven LE. Coating flow theory by finite element and asymptotic analysis of the Navier-Stokes system. *Int J Num Meth Fluids*. 1984;4:207–229.
13. Hirt CW, Amsden AA, Cook JL. An arbitrary Lagrangian-Eulerian computing method for all flow speeds. *J Comp Phys*. 1974;14:227–253.
14. Dimakopoulos Y, Tsamopoulos J. A quasi-elliptic transformation for moving boundary problems with large anisotropic deformations. *J Comp Phys*. 2003;192:494–522.
15. Hirt CW, Nichols BD. Volume of fluid (VOF) method for the dynamics of free boundaries. *J Comput Phys*. 1981;39:201–225.
16. Osher SJ, Sethian JA. Fronts propagating with curvature-dependent speed - algorithms based on Hamilton-Jacobi formulations. *J Comput Phys*. 1988;79:12–49.
17. Bird RB, Dai GC, Yarusso BJ. The rheology and flow of viscoplastic materials. *Rev Chem Eng*. 1982;1:1–70.
18. Mitsoulis E. Numerical simulation of fountain flow of pseudoplastic and viscoplastic fluids. Submitted to *J Non-Newtonian Fluid Mech*. 2009.
19. Taliadorou E, Georgiou GC, Mitsoulis E. Numerical simulation of the extrusion of strongly compressible Newtonian liquids. *Rheol. Acta*. 2008;47:49–62.
20. Huilgol RR, You Z. On the importance of the pressure dependence of viscosity in steady nonisothermal shearing flows of compressible and incompressible fluids and in the isothermal fountain flow. *J Non-Newtonian Fluid Mech*. 2006;136:106–117.

21. Cardinaels R, Van Puyvelde P, Moldenaers P. Evaluation and comparison of routes to obtain pressure coefficients from high-pressure capillary rheometry data. *Rheol Acta*. 2007;46:495–505.
22. Mitsoulis E. Annular extrudate swell of Newtonian fluids: effects of compressibility and slip at the wall. *J Fluids Eng*. 2007;129:1384–1393.
23. Georgiou GC, Boudouvis AG. Converged solutions for the Newtonian extrudate-swell problem. *Int J Numer Meth Fluids*. 1999; 29:363–371.
24. Georgiou G. Annular liquid jets at high Reynolds numbers. *Int J Numer Meth Fluids*. 2003;42:117–130.
25. Mitsoulis E, Vlachopoulos J. The finite element method for fluid flow and heat transfer analysis. *Adv Polym Technol*. 1984;4:107–121.
26. Lee S-L, Liao W-C. Numerical simulation of a fountain flow on nonstaggered cartesian grid system. *Int J Heat Mass Transfer*. 2008; 51:2433–2443.
27. Georgiou GC, Crochet MJ. Compressible viscous flow in slits, with slip at the wall. *J Rheol*. 1994;38:639–654.
28. Mitsoulis E. Annular extrudate swell of Newtonian fluids revisited: Extended range of compressible simulations. *J Fluids Eng*. 2009; 131:071203-1-10.
29. Mavridis H. Finite Element Studies in Injection Mold Filling. Dept. Chem. Eng., McMaster University, Hamilton, ON, Canada; 1988. PhD Thesis.

Manuscript received May 10, 2009, and revision received July 8, 2009.